Check for updates

Angewandte Chemie International Edition

Angewandte International Edition Chemie

How to cite: *Angew. Chem. Int. Ed.* **2026**, e3793292
doi.org/10.1002/anie.3793292

RESEARCH ARTICLE Hot Paper

Low-Crystalline $Ag_{1.2}V_3O_8$: A Zinc-Ion Storage Cathode With an Ultrahigh Capacity of 525 mAh g^{-1} Enabled by Oxygen-Vacancy-Rich Coordination Environments

Hongxuan Tang[1,4] | Lixun Feng[1] | Xiaoyue Li[3] | Cuiqin Chao[1] | Longlong Tian[1] | Xiaojun Gu[1] | Jiahuan Zhao[2] | Xiaoying Liu[1] | Lifang Zheng[1] | Yuan Chen[1] | Yan Zhao[1] | Jiangwei Zhang[1] | Linfeng Hu[3] | Limin Wu[1,2]

[1]College of Energy Materials and Chemistry; School of Physical Science and Technology, Inner Mongolia University, Hohhot, Inner Mongolia, China | [2]College of Smart Materials and Future Energy, State Key Laboratory of Coatings for Advanced Equipment and Advanced Coatings Research Center of Ministry of Education of China, Fudan University, Shanghai, China | [3]School of Materials Science and Engineering, Southeast University, Nanjing, China | [4]Key Laboratory of Ocean Energy Utilization and Energy Conservation of Ministry of Education, School of Energy and Power Engineering, Dalian University of Technology, Dalian, China

Correspondence: Yan Zhao (yanzhao@imu.edu.cn) | Linfeng Hu (linfenghu@seu.edu.cn) | Limin Wu (wlm@fudan.edu.cn)

Received: 7 July 2026 | **Revised:** 7 September 2026 | **Accepted:** 9 September 2026

Keywords: aqueous zinc-ion battery | dual-redox chemistry | low-crystalline silver vanadate | oxygen vacancy | pseudocapacitive zinc-ion storage

ABSTRACT

Conventional vanadium-based cathodes are limited by sluggish Zn^{2+} transport, poor electronic conductivity, and incomplete utilization of redox-active sites. Here, redox-active Ag serves as a regulator of local coordination chemistry in a short-range-ordered low-crystalline vanadate. Ag incorporation reconstructs the local Ag-V-O environment, lowers the oxygen-vacancy formation energy, promotes V^{5+}/V^{4+} conversion, and activates electrochemically accessible Ag/V dual-redox centers, thereby simultaneously enhancing electronic accessibility and Zn^{2+} transport kinetics. Meanwhile, the short-range-ordered low-crystalline framework stabilizes these defect-rich coordination environments, provides pseudocapacitive-favored charge-storage pathways, and accommodates local structural strain during repeated Zn^{2+} insertion/extraction. Density functional theory (DFT) calculations reveal that Ag incorporation markedly reduces the Zn^{2+} migration barrier and increases electronic states near the Fermi level. Consequently, the low-crystalline silver vanadate cathode delivers an ultrahigh reversible capacity of 525.51 mAh g^{-1} at 0.1 A g^{-1}, a high energy density of 499.23 Wh kg^{-1}, excellent rate capability, and outstanding cycling stability with 96.2% capacity retention after 5,000 cycles at 8 A g^{-1}. This work demonstrates that local coordination reprogramming unlocks Ag/V redox chemistry and pseudocapacitive Zn^{2+} storage, highlighting a promising strategy for enhancing redox accessibility and Zn-ion storage in low-crystalline vanadate cathodes.

1 | Introduction

Aqueous zinc-ion batteries (AZIBs) are emerging as promising candidates for safe and cost-effective electrochemical energy storage because of the intrinsic safety of aqueous electrolytes, the high theoretical capacity of metallic zinc, and the natural abundance of zinc resources [1–3]. Despite these advantages, the practical energy output of AZIBs is still largely limited by the cathode side, where sluggish multivalent-ion diffusion, insufficient electronic conductivity, structural degradation, and incomplete utilization of redox-active centers commonly lead to limited capacity and poor rate capability [4]. Developing cathode

All rights reserved, including rights for text and data mining and training of artificial intelligence technologies or similar technologies.
© 2026 Wiley-VCH GmbH

materials that can simultaneously deliver high capacity, fast kinetics, and long-term structural reversibility remains a central challenge for high-energy AZIBs [5, 6].

Among the reported cathode candidates, vanadium-based oxides and vanadates have attracted particular attention because their multiple V oxidation states, flexible V-O polyhedral coordination, and tunable layered or tunnel-like frameworks can support multi-electron charge storage [7, 8]. However, conventional crystalline vanadates usually rely on bulk Zn^{2+} or H^+ insertion/extraction reactions, which are kinetically constrained by strong electrostatic interactions between divalent Zn^{2+} ions and rigid host lattices. Repeated insertion of hydrated Zn^{2+} ions and protons can also induce lattice distortion, vanadium dissolution, phase reconstruction, and gradual loss of accessible redox sites [9]. For most single-metal vanadium oxides, these drawbacks translate into limited practical capacity (typically, <400 mAh g^{-1} at <0.5 A g^{-1}) and poor rate performance (over 50% fade at 0.1 to 5 A g^{-1}) [10–12]. These limitations indicate that merely constructing a stable crystalline host is insufficient for achieving ultrahigh-capacity Zn-ion storage. Instead, the key issue is how to maximize the electrochemical accessibility of redox-active sites while maintaining fast ion transport and structural adaptability [7, 9].

Recent studies have shown that capacities beyond conventional bulk-intercalation limits can be achieved when surface or near-surface redox sites, defect-mediated storage sites, and pseudocapacitive Faradaic reactions are effectively activated [1, 13, 14]. In this context, structural disorder, amorphous domains, and defect engineering provide powerful routes to weaken local ion-diffusion barriers, increase electrochemically accessible active sites, and buffer local strain during repeated ion insertion [1, 15]. Nevertheless, excessive amorphization may sacrifice structural integrity and aggravate irreversible reconstruction during long-term cycling [15]. Therefore, an ideal vanadate cathode should not simply maximize disorder, but should construct a short-range ordered low-crystalline framework that combines the kinetic advantages of local disorder with the structural robustness of an oxide backbone.

Silver-containing vanadates offer an additional opportunity because Ag species can participate in reversible Ag^+/Ag^0 redox chemistry and modulate the electronic structure of the vanadate host [16]. Previous studies on crystalline silver vanadates have revealed that Ag-related redox reactions and in situ generated metallic Ag can enhance electrical conductivity and improve rate performance [17]. However, these systems are generally based on well-defined crystalline frameworks, where rigid lattice environments, irreversible displacement reactions, or limited defect accessibility restrict the full utilization of Ag/V redox chemistry. Thus, a critical but rarely explored question is whether redox-active Ag species can be incorporated into a low-crystalline vanadate framework to simultaneously reprogram local defect chemistry, electronic structure, and Zn^{2+} transport pathways.

Here, we develop a low-crystalline $Ag_{1.2}V_3O_8$ cathode, denoted LC-$Ag_{1.2}V_3O_8$, in which Ag incorporation and short-range ordered structural disorder cooperatively unlock ultrahigh-capacity aqueous Zn-ion storage. The high-crystalline counterpart, denoted HC-$Ag_{1.2}V_3O_8$, is used as a direct reference to decouple the role of low crystallinity from the intrinsic Ag-containing vanadate composition. Distinct from conventional intercalation or dilute doping strategies, Ag is incorporated as an electronically and electrochemically active constituent within the Ag-V-O coordination environment. Ag incorporation induces partial reduction of V^{5+} to V^{4+}, lowers the oxygen-vacancy formation energy, and generates Ag/V dual redox centers, thereby increasing the density of electronic states near the Fermi level and accelerating charge transfer. Meanwhile, the short-range ordered low-crystalline domains preserve flexible local coordination, abundant diffusion pathways, and electrochemically accessible defect-rich Ag-V-O coordination environments, which collectively facilitate rapid Zn^{2+} transport, pseudocapacitive Faradaic charge storage, and structural-strain accommodation during cycling. Benefiting from these coupled effects, LC-$Ag_{1.2}V_3O_8$ delivers a much higher reversible capacity of 525.51 mAh g^{-1} at 0.1 A g^{-1}, a superior energy density of 499.23 Wh kg^{-1}, and outstanding cycling stability over 5,000 cycles at 8 A g^{-1}. Density functional theory (DFT) calculations further show that Ag incorporation lowers oxygen-vacancy formation energy and increases the electronic states near the Fermi level, providing a mechanistic basis for the enhanced Zn^{2+} storage capability. Collectively, this work identifies Ag-enabled defect and electronic reprogramming in low-crystalline vanadates as an effective strategy for enhancing Ag/V redox accessibility, accelerating Zn^{2+} transport, and promoting high-capacity aqueous Zn-ion storage.

2 | Results and Discussion

2.1 | Structural Evolution, Phase Formation, and Defect Chemistry

The precursor containing $[V_xO_y]^{n-}$ polyanions was synthesized through a modified co-precipitation process (Figure 1a). Briefly, V_2O_5 was dissolved in dilute H_2O_2 to form a vanadate solution, which was aged under stirring to decompose excess peroxide. Subsequently, an $AgNO_3$ aqueous solution was introduced into the vanadate precursor, and the pH was carefully adjusted to 1.8 using dilute nitric acid. Slow evaporation of the mixed solution at room temperature led to the formation of a silver-vanadium oxide composite, where the electrostatic interaction between Ag^+ ions and polyvanadate anions promoted the incorporation of Ag into the vanadate framework. To further confirm the structural evolution, the as-obtained LC-$Ag_{1.2}V_3O_8$ was annealed at 350°C under an Ar atmosphere to obtain its high-crystalline counterpart, denoted HC-$Ag_{1.2}V_3O_8$. The sharp x-ray diffraction (XRD) reflections of HC-$Ag_{1.2}V_3O_8$ confirm the formation of a well-defined crystalline Ag-V-O framework. In contrast, the as-synthesized LC-$Ag_{1.2}V_3O_8$ displayed broad diffraction peaks and no distinct Ag-related reflections (Figure 1b), confirming its predominantly low-crystalline nature without detectable crystalline Ag-containing phases. The absence of sharp reflections and the slight shift of the (011) plane relative to $H_2V_3O_8$ (HVO) suggest Ag^+-induced rearrangement of vanadate clusters (Figure S1).

Inductively coupled plasma atomic emission spectroscopy (ICP-AES) gives an Ag:V atomic ratio of 1:2.72 (Table S1), validating the designed composition. X-ray photoelectron spectroscopy (XPS) further differentiated LC-$Ag_{1.2}V_3O_8$, HC-$Ag_{1.2}V_3O_8$, and pristine HVO (Figure 1c). The Ag 3d spectra show that Ag is

15213773, 0, Downloaded from https://onlinelibrary.wiley.com/doi/10.1002/anie.3793292 by Hu linfeng - Southeast University , Wiley Online Library on [19/09/2026]. See the Terms and Conditions (https://onlinelibrary.wiley.com/terms-and-conditions) on Wiley Online Library for rules of use; OA articles are governed by the applicable Creative Commons License

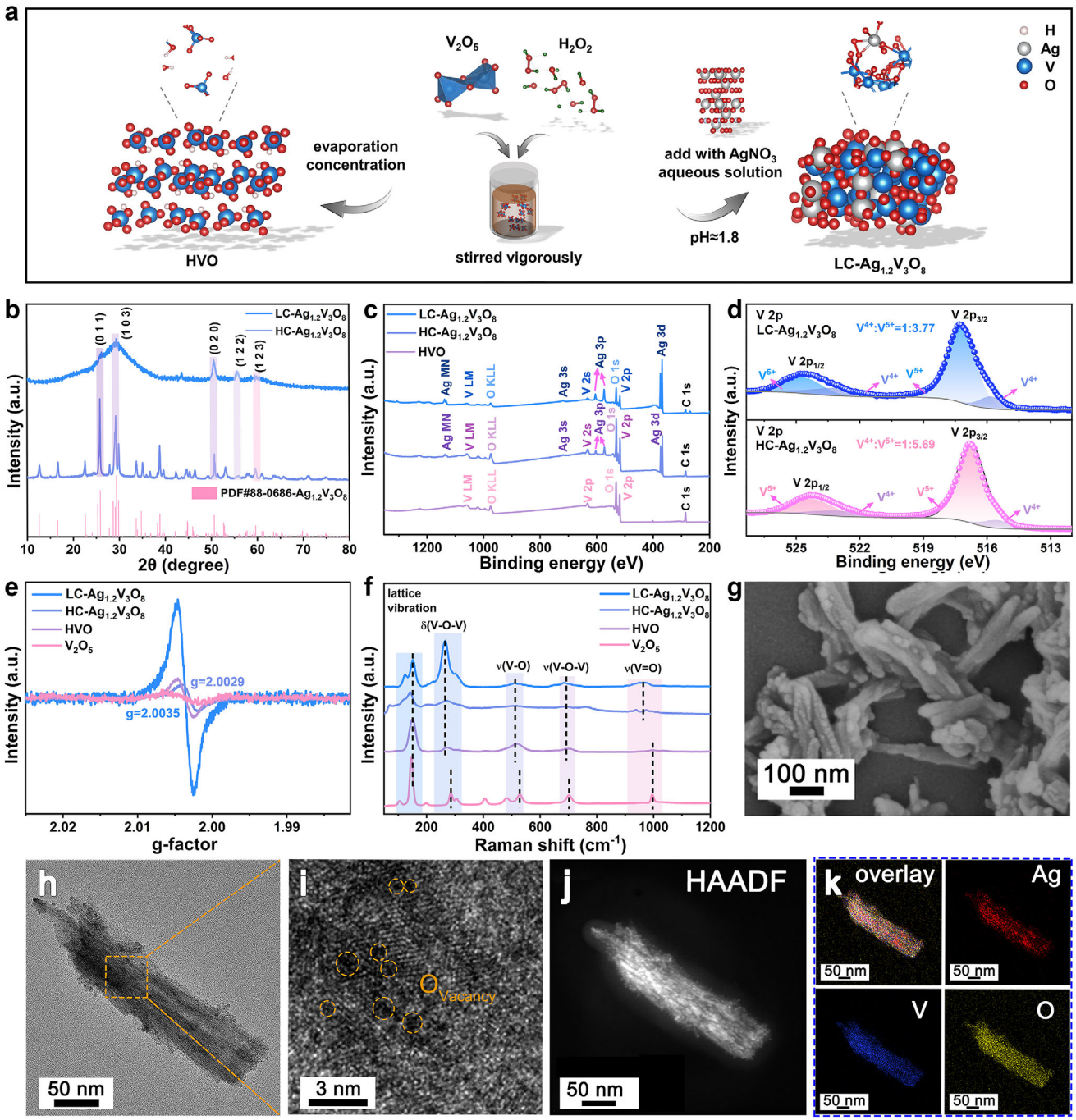

FIGURE 1 | Structural and compositional characterization of LC-$Ag_{1.2}V_3O_8$. (a) Schematic formation process. (b) XRD patterns of LC-$Ag_{1.2}V_3O_8$ and HC-$Ag_{1.2}V_3O_8$. (c) XPS survey spectra of LC-$Ag_{1.2}V_3O_8$, HC-$Ag_{1.2}V_3O_8$, and HVO. (d) High-resolution V 2p XPS spectrum of LC-$Ag_{1.2}V_3O_8$ and HC-$Ag_{1.2}V_3O_8$. (e) EPR and (f) Raman spectra of LC-$Ag_{1.2}V_3O_8$, HC-$Ag_{1.2}V_3O_8$, HVO, and V_2O_5. (g–i) SEM, TEM, and HRTEM images of LC-$Ag_{1.2}V_3O_8$. (j, k) HAADF image and corresponding EDS elemental maps of Ag, V, and O.

predominantly present in an oxidized state in both LC-$Ag_{1.2}V_3O_8$ and HC-$Ag_{1.2}V_3O_8$, confirming successful incorporation into the vanadate framework rather than metallic Ag formation (Figures S2 and S3). High-resolution V 2p spectra revealed the mixed states of V^{5+}/V^{4+}, with a dominant V^{5+} component consistent with the proposed stoichiometry (Figure 1d) [18]. The O 1s spectra (Figures S4 and S5) displayed a strong defect-related signal at ~531.5 eV for LC-$Ag_{1.2}V_3O_8$, indicative of abundant oxygen vacancies, whereas this feature was significantly weakened after crystallization [19].

Electron paramagnetic resonance (EPR) spectroscopy (Figure 1e) provided further evidence of defect formation. Since V^{4+} is paramagnetic whereas V^{5+} is EPR-silent [20], the signal intensity directly reflects the concentration of reduced vanadium and associated oxygen vacancies [21]. LC-$Ag_{1.2}V_3O_8$ exhibited a g-value of 2.0035 and an order-of-magnitude stronger signal intensity than HVO and HC-$Ag_{1.2}V_3O_8$, revealing a higher concentration of V^{4+} species and oxygen vacancies [20]. The larger g-shift relative to the crystalline sample (HC-$Ag_{1.2}V_3O_8$: g-value = 2.0029) further

15213773, 0, Downloaded from https://onlinelibrary.wiley.com/doi/10.1002/anie.3793292 by Hu linfeng - Southeast University , Wiley Online Library on [19/09/2026]. See the Terms and Conditions (https://onlinelibrary.wiley.com/terms-and-conditions) on Wiley Online Library for rules of use; OA articles are governed by the applicable Creative Commons License

indicates that LC-$Ag_{1.2}V_3O_8$ possesses a more disordered and defect-rich local environment [22]. Raman (Figure 1f) and FT-IR (Figure S6) spectra retained the characteristic V-O vibrations of the vanadate framework, but both exhibited noticeable band shifts after Ag incorporation, indicating local bonding perturbations while maintaining the overall framework integrity [23]. Zeta-potential measurements (Figure S7) reveal a marked difference in the surface-charge environment of LC-$Ag_{1.2}V_3O_8$ relative to HVO, consistent with the altered defect-rich surface chemistry independently supported by XPS and EPR [24].

Scanning electron microscopy (SEM) and transmission electron microscopy (TEM) images (Figure 1g-i; Figures S8 and S9) reveal interconnected rod-like nanostructures with uniformly dispersed nanoscale domains within the vanadate matrix. Compared with HC-$Ag_{1.2}V_3O_8$, HVO, V_2O_5 (Figures S10–S13), LC-$Ag_{1.2}V_3O_8$ displays small particle sizes and a more homogeneous distribution, features that are advantageous for uniform electrochemical reactions. High-angle annular dark-field (HAADF) image (Figure 1j) and energy-dispersive x-ray spectroscopy (EDS) mapping images (Figures 1k and S14) further confirm the uniform distribution of Ag, V, and O throughout the composite. Brunauer-Emmett-Teller (BET) measurements reveal that LC-$Ag_{1.2}V_3O_8$ exhibits a substantially enhanced surface area relative to pristine vanadates, furnishing profuse active sites for electrochemical reactions (Figure S15) [25]. High-resolution TEM (HRTEM) imaging (Figure 1i) reveals locally disordered lattice regions consistent with the presence of oxygen vacancies, in line with XPS and EPR results. The corresponding inverse fast Fourier transform (FFT) image (Figure S16) highlights lattice distortions associated with Ag incorporation and defect formation. Density functional theory (DFT, Figure S17) calculations further substantiate these findings. The oxygen vacancy formation energy of LC-$Ag_{1.2}V_3O_8$ (1.97 eV) is much lower than that of pristine HVO (3.99 eV), while crystalline HC-$Ag_{1.2}V_3O_8$ shows an intermediate value (2.8 eV). This comparison demonstrates that Ag incorporation lowers the energy barrier for defect formation, and that structural disorder in the low-crystalline phase further amplifies this effect. Collectively, these results show that Ag incorporation does not simply introduce a secondary component, but reconfigures the local Ag-V-O coordination and stabilizes oxygen-vacancy-rich low-crystalline domains that are inherently favorable for charge transport and Zn^{2+} accessibility.

2.2 | Local Coordination Reconstruction and Electronic Structure Modulation

X-ray absorption near-edge structure (XANES) and extended x-ray absorption fine structure (EXAFS) analyses provide detailed information on the coordination environment of vanadium and silver in LC-$Ag_{1.2}V_3O_8$ (Tables S2 and S3; Figures S18–S25). At the V K-edge (Figures 2a and S20), the absorption threshold of LC-$Ag_{1.2}V_3O_8$ shifts by ~1.47 eV toward lower energy relative to V_2O_5, accompanied by a marked decrease in white-line intensity. These features indicate partial reduction of V^{5+} to V^{4+}, consistent with the V^{5+}/V^{4+} ratio (3.77:1) and average valence state (+4.79) obtained from XPS. Such mixed-valence V centers are expected to enhance redox accessibility and facilitate charge storage. Fourier-transformed k^2-weighted EXAFS spectra (Figure 2b) show that the main V-O peak (~2.13 Å) decreases in intensity (~3.2%) and broadens in full width at half maximum compared with HVO, indicating increased structural disorder and local lattice distortion. This disorder is attributed to oxygen vacancies and asymmetric rearrangement of VO_6 octahedra. Wavelet transform (WT) EXAFS (Figures 2c and S21) further highlights signal attenuation and shifts ($k \approx 6.7$ Å^{-1} and $R \approx 1.7$ Å), evidencing bond-length disorder and reconstruction of the V-O coordination environment. Importantly, the EXAFS fitting identifies V-O-V (~3.29 Å) and V-O-Ag (~3.36 Å) multiple-scattering paths, demonstrating that Ag is incorporated into the vanadate framework rather than segregating as a secondary phase.

At the Ag K-edge, the XANES spectrum of LC-$Ag_{1.2}V_3O_8$ (Figure 2d,e) is slightly shifted relative to Ag_2O, while the enhanced white-line intensity indicates that Ag mainly exists in a low-valence oxidized state coordinated with oxygen (Figure S24). FT-EXAFS and WT-EXAFS analyses (Figures S23 and S25) further identify Ag-O and Ag-V contributions, confirming strong local coupling between Ag and the vanadate host. Differential charge-density calculations (Figure 2f) reveal pronounced electron accumulation around Ag, suggesting active participation in charge redistribution across the Ag-V-O framework. First-principles calculations further show that LC-$Ag_{1.2}V_3O_8$ possesses a substantially higher electronic state density near the Fermi level (E_F) than HC-$Ag_{1.2}V_3O_8$ and HVO (Figure 2g,h), indicating enhanced electronic accessibility. Notably, Ag 3d orbitals make a significant contribution to the states near E_F and become delocalized in the low-crystalline phase, imparting enhanced electronic delocalization to the framework. Together, these synchrotron and computational results reveal that Ag is not a passive guest species, but an electronically active constituent that participates in local Ag-V-O coordination, stabilizes oxygen-vacancy-rich mixed-valence environments, and increases the density of accessible states near the Fermi level. This Ag-enabled reprogramming of local coordination and electronic structure provides the basis for the exceptional Zn^{2+} storage capability of LC-$Ag_{1.2}V_3O_8$.

2.3 | Electrochemical Storage Behavior and Redox Activity

The cyclic voltammetry (CV) profiles of the LC-$Ag_{1.2}V_3O_8$ electrode within the voltage range of 0.2-1.7 V at a scan rate of 0.2 mV s^{-1} (Figures 3a and S26) exhibit several well-defined redox couples, corresponding to Zn^{2+} intercalation/deintercalation and multi-electron transitions of vanadium and silver. The redox couple at 0.52/0.68 V versus Zn^{2+}/Zn and the redox peaks located at 0.76, 0.91, and 1.02 V are associated with stepwise Zn^{2+} insertion/extraction within the V-O layered framework, accompanied by $V^{5+}/V^{4+}/V^{3+}$ redox transitions [21, 26]. The redox couple at 1.10/1.41 V versus Zn^{2+}/Zn can be assigned to the Ag^0/Ag^+ redox couple [16], consistent with the dQ/dV analysis (Figure S27). Moreover, the relatively narrow potential separation (ΔE) between the oxidation and reduction peaks implies low polarization and enhanced redox kinetics, suggesting that Ag incorporation effectively improves the electronic conductivity and facilitates rapid Zn^{2+} diffusion within the electrode matrix.

Galvanostatic charge-discharge (GCD) profiles exhibit characteristic sloping plateaus, reflecting the synergistic contributions

15213773, 0, Downloaded from https://onlinelibrary.wiley.com/doi/10.1002/anie.3793292 by Hu linfeng - Southeast University , Wiley Online Library on [19/09/2026]. See the Terms and Conditions (https://onlinelibrary.wiley.com/terms-and-conditions) on Wiley Online Library for rules of use; OA articles are governed by the applicable Creative Commons License

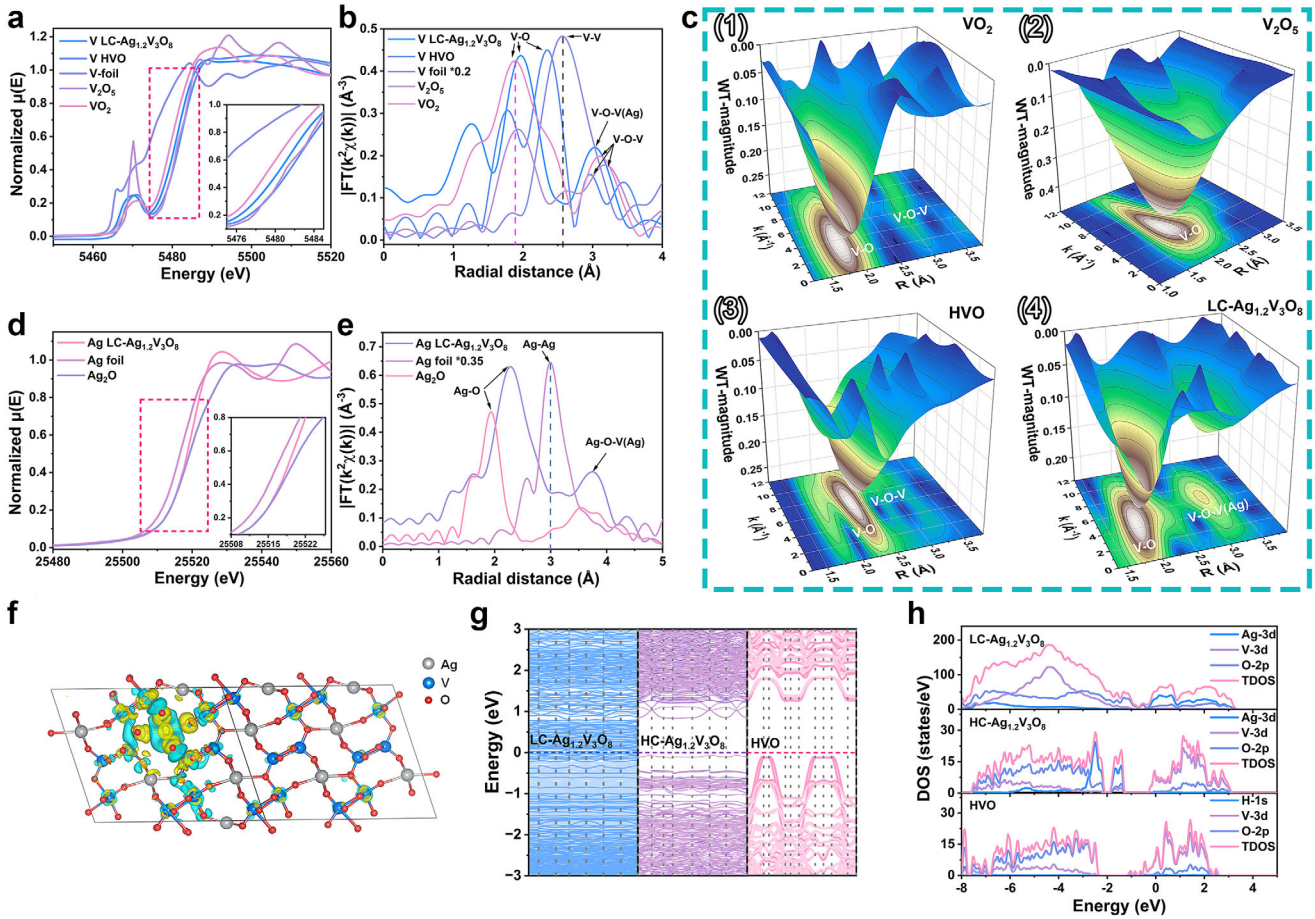

FIGURE 2 | Local structural and electronic characterization of LC-$Ag_{1.2}V_3O_8$. (a) V K-edge XANES spectra. (b) Fourier-transformed (FT) EXAFS spectra of V K-edge in R-space. (c) Wavelet transform (WT) EXAFS analyses of (1) VO_2, (2) V_2O_5, (3) HVO, and (4) LC-$Ag_{1.2}V_3O_8$. (d) Ag K-edge XANES spectra. (e) FT-EXAFS spectra of Ag K-edge. (f) Differential charge density of LC-$Ag_{1.2}V_3O_8$. (g) Band structure and (h) Density of states (DOS) of LC-$Ag_{1.2}V_3O_8$, HC-$Ag_{1.2}V_3O_8$, and HVO.

of Ag^+/Ag^0 and vanadium-based redox reactions (Figure S28). The LC-$Ag_{1.2}V_3O_8$ electrode delivers average capacities of 525.51, 490.81, 480.31, 470.92, 411.48, 397.99, and 298.73 mAh g^{-1} at current densities of 0.1, 0.2, 0.3, 0.5, 1.0, 3.0, and 5.0 A g^{-1}, respectively, which are much higher than those of HC-$Ag_{1.2}V_3O_8$, HVO, and V_2O_5 (Figure S29). At 0.1 A g^{-1}, the LC-$Ag_{1.2}V_3O_8$//Zn cell demonstrates minimal voltage hysteresis (ΔV = 0.1251 V) between charge (0.9348 V) and discharge (0.8097 V) plateaus, significantly lower than HC-$Ag_{1.2}V_3O_8$ (ΔV = 0.2755 V), HVO (ΔV = 0.5251 V) and V_2O_5 (ΔV = 0.4628 V) (Figure 3b). This low polarization is further attributed to the electronically accessible Ag-V-O framework, which facilitates rapid electron transfer and provides additional redox-active sites, reducing overpotentials and enhancing reaction reversibility [6]. Compared with HC-$Ag_{1.2}V_3O_8$, HVO, and V_2O_5, the LC-$Ag_{1.2}V_3O_8$ electrode exhibits markedly higher specific capacity, underscoring the cooperative effects of Ag incorporation, defect enrichment, and low-crystalline structural adaptation. Furthermore, as shown in Figure 3c and Table S4, the LC-$Ag_{1.2}V_3O_8$ cathode demonstrates a higher specific capacity than other vanadium-based systems. The comparison of energy and power densities (Figure 3d) shows that LC-$Ag_{1.2}V_3O_8$ achieves 499.23 Wh kg^{-1} (based on cathode mass), outperforming most advanced vanadium-based AZIBs reported. The radar plot (Figure 3e) further highlights the well-balanced and superior overall performance of LC-$Ag_{1.2}V_3O_8$ across multiple metrics, markedly surpassing HC-$Ag_{1.2}V_3O_8$, HVO, and V_2O_5 (Figure S29). The exceptional durability of LC-$Ag_{1.2}V_3O_8$ is further evidenced by long-term cycling. It achieves the highest capacity at 0.2 A g^{-1} (Figure 3f) and shows almost no capacity fading after 5,000 cycles at 8.0 A g^{-1}, surpassing HC-$Ag_{1.2}V_3O_8$, HVO, and V_2O_5 (Figure 3g). The unusually high capacity of LC-$Ag_{1.2}V_3O_8$ is attributed to the synergistic effects of Ag/V dual-redox chemistry, defect-rich coordination environments, enhanced pseudocapacitive storage, and rapid Zn^{2+} transport enabled by Ag-induced structural and electronic modulation. Representative charge/discharge profiles collected over selected late-stage cycle windows (cycles 1000, 2000, 3000, 4000, and 5000) retain similar overall shapes with no pronounced profile distortion, indicating stable reaction characteristics during prolonged cycling (Figure S30).

To further evaluate its practical applicability, LC-$Ag_{1.2}V_3O_8$ was assembled into pouch-cell configuration (Figure S31). The pouch cell exhibits electrochemical behavior consistent with that of the coin cell, and the corresponding CV curves display three pairs of redox peaks, confirming reversible Zn^{2+} storage. Using a 3 cm × 4 cm LC-$Ag_{1.2}V_3O_8$ cathode (area: 12 cm^2), the pouch cell delivers a specific capacity of 463.36 mAh g^{-1} at 0.5 A g^{-1} and maintains

15213773, 0, Downloaded from https://onlinelibrary.wiley.com/doi/10.1002/anie.3793292 by Hu linfeng - Southeast University , Wiley Online Library on [19/09/2026]. See the Terms and Conditions (https://onlinelibrary.wiley.com/terms-and-conditions) on Wiley Online Library for rules of use; OA articles are governed by the applicable Creative Commons License

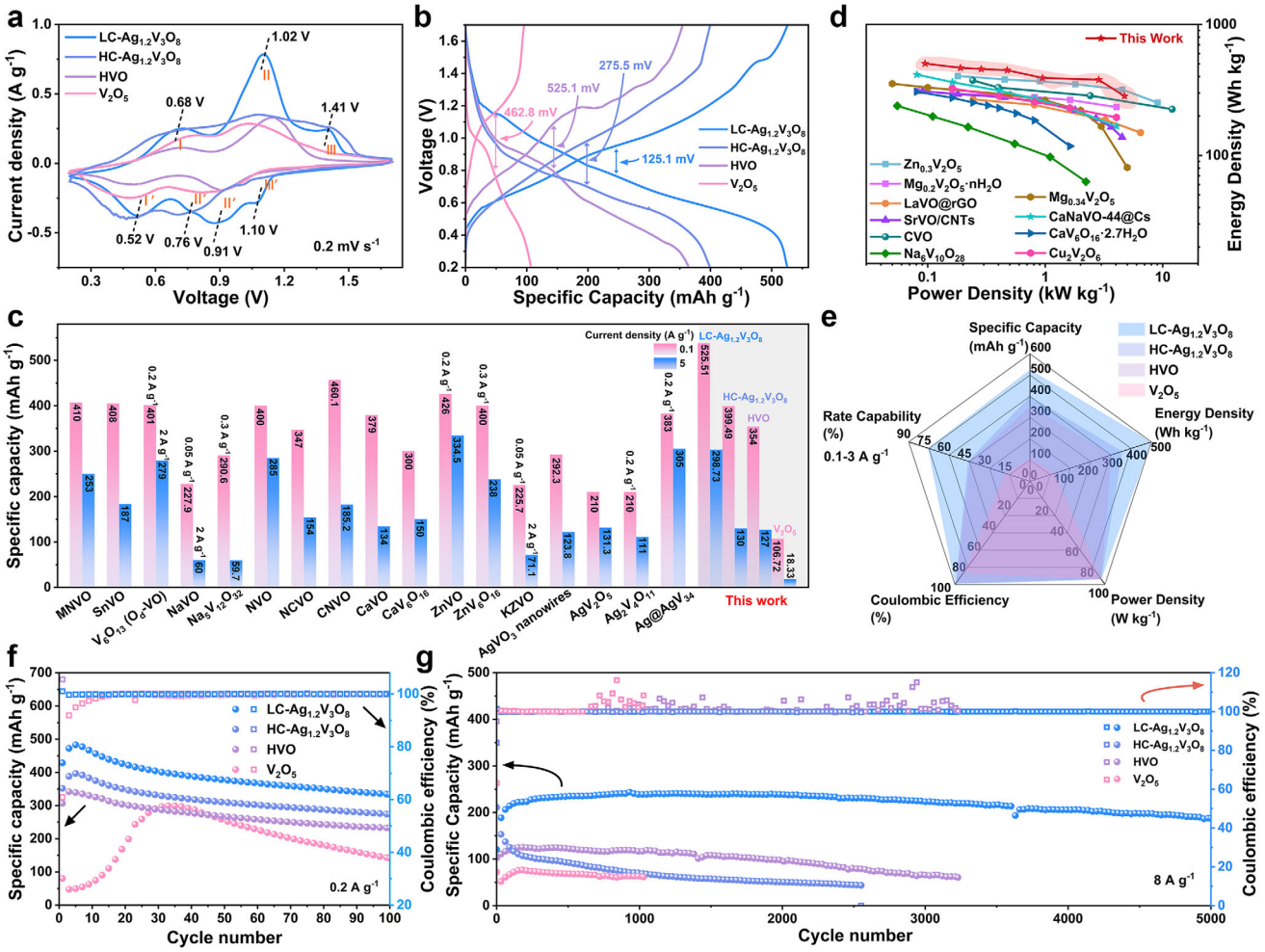

FIGURE 3 | Electrochemical performance of LC-$Ag_{1.2}V_3O_8$, HC-$Ag_{1.2}V_3O_8$, HVO, and V_2O_5 electrodes. (a) CV curves at 0.2 mV s^{-1}. Comparison of (b) GCD curves, (c) specific capacity between LC-$Ag_{1.2}V_3O_8$//Zn battery and previously reported vanadium-based Zn-ion batteries [4–6, 10, 11, 16, 27–38], (d) Ragone plot comparing the power and energy densities of LC-$Ag_{1.2}V_3O_8$//Zn with other Zn batteries [4, 6, 12, 31, 38–44], and (e) comprehensive performance. Long-term cycling performance of LC-$Ag_{1.2}V_3O_8$, HC-$Ag_{1.2}V_3O_8$, HVO, and V_2O_5 electrodes at (f) 0.2 A g^{-1} and (g) 8 A g^{-1}.

80.61% capacity retention over 30 cycles. Moreover, three pouch cells connected in series successfully powered a 5 V LED array, highlighting the practical scalability of the LC-$Ag_{1.2}V_3O_8$ cathode.

2.4 | Kinetic Origin and Zn^{2+} Diffusion Mechanism

To clarify why LC-$Ag_{1.2}V_3O_8$ can sustain such unusually deep and reversible Zn^{2+} storage, we next examined the relative contributions of capacitive and diffusion-controlled processes, together with Zn^{2+} transport dynamics and migration energetics. CV curves recorded at scan rates of 0.2 to 1.0 mV s^{-1} (Figure 4a) preserve their overall profiles while exhibiting progressively increased peak currents and slight peak shifts, indicating polarization under fast kinetics. Linear fitting of log(i) versus log(v) (Figure 4b and Equation S1) yielded b-values between 0.5–1.0 for all redox peaks, indicating a hybrid storage mechanism involving both diffusion-limited intercalation and capacitive processes. The capacitive contribution increases with scan rate and reaches 75.47% at 1.0 mV s^{-1} for LC-$Ag_{1.2}V_3O_8$ (Figures 4c and S32; Equation S2), indicating pronounced pseudocapacitive charge-storage behavior. Notably, this value is much higher than that of HC-$Ag_{1.2}V_3O_8$ under the same condition (50.89% at 1.0 mV s^{-1}), suggesting that the LC-$Ag_{1.2}V_3O_8$ framework enables greater accessibility of reversible Ag/V redox centers than its crystalline counterpart. Previous studies on ultrathin, defect-rich, or structurally disordered oxide electrodes have shown that highly exposed surface/near-surface sites and capacitive Faradaic reactions can provide additional charge-storage contributions beyond conventional bulk intercalation, while reducing ion-transport limitations associated with rigid crystalline frameworks [13–15, 45]. Combined with the oxygen-vacancy-rich coordination environments revealed by XPS, EPR, and DFT calculations, this enhanced capacitive response indicates that defect-rich Ag-V-O coordination environments contribute to the rapid charge-storage kinetics and unusually high capacity of LC-$Ag_{1.2}V_3O_8$.

To further probe ion-transport kinetics, electrochemical impedance spectroscopy (EIS) (Figure 4d) and galvanostatic intermittent titration technique (GITT) (Figures 4e and S33) were employed. The Nyquist plots reveal that LC-$Ag_{1.2}V_3O_8$ possesses a markedly lower charge-transfer resistance (R_{ct}) than the comparison electrodes, indicating more favorable interfacial

15213773, 0, Downloaded from https://onlinelibrary.wiley.com/doi/10.1002/anie.3793292 by Hu linfeng - Southeast University , Wiley Online Library on [19/09/2026]. See the Terms and Conditions (https://onlinelibrary.wiley.com/terms-and-conditions) on Wiley Online Library for rules of use; OA articles are governed by the applicable Creative Commons License

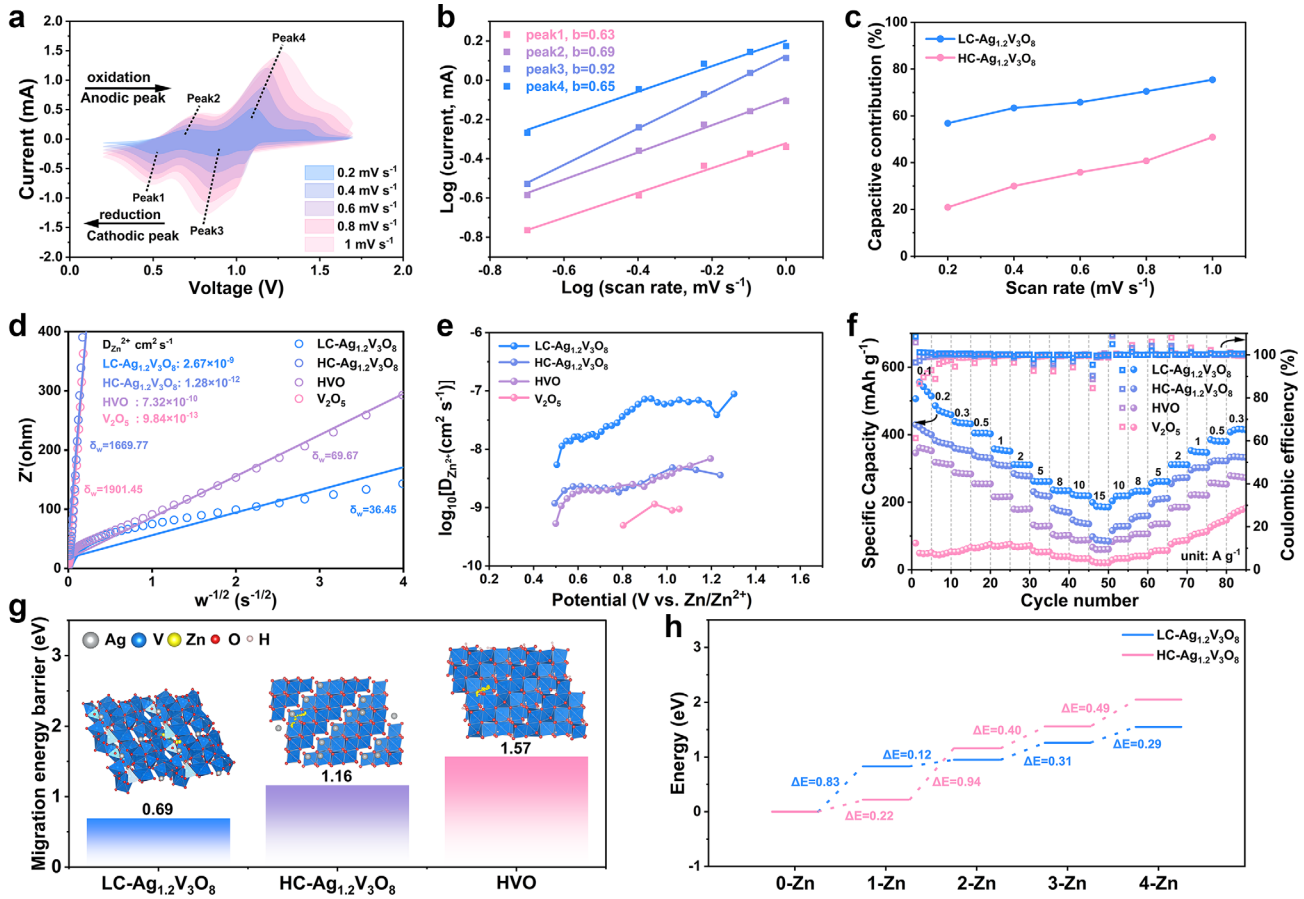

FIGURE 4 | Electrochemical kinetics and Zn^{2+} diffusion behavior of LC-$Ag_{1.2}V_3O_8$. (a) CV curves at various scan rates. (b) Corresponding plots of log(i) versus log(v) for the four redox peaks in (a), with slopes representing the b-values. (c) Capacitive contributions of LC-$Ag_{1.2}V_3O_8$ and HC-$Ag_{1.2}V_3O_8$ at various scan rates. (d) EIS-calculated Zn^{2+} diffusion coefficient. (e) GITT-derived $D_{Zn}{}^{2+}$ comparison among LC-$Ag_{1.2}V_3O_8$, HC-$Ag_{1.2}V_3O_8$, HVO, and V_2O_5. (f) Rate capability. (g) Diffusion pathways and corresponding migration barriers of Zn^{2+} in LC-$Ag_{1.2}V_3O_8$, HC-$Ag_{1.2}V_3O_8$, and HVO. (h) Calculated Zn^{2+} insertion energies as a function of Zn content for LC-$Ag_{1.2}V_3O_8$ and HC-$Ag_{1.2}V_3O_8$.

charge-transfer kinetics. The diffusion coefficients (D) calculated from EIS (Equations S3 and S4) reach 2.67×10^{-9} cm^2 s^{-1} for LC-$Ag_{1.2}V_3O_8$, significantly surpassing those of HC-$Ag_{1.2}V_3O_8$ (1.28×10^{-12} cm^2 s^{-1}), HVO (7.32×10^{-10} cm^2 s^{-1}), and V_2O_5 (9.84×10^{-13} cm^2 s^{-1}). GITT analysis reveals the same trend as EIS, with LC-$Ag_{1.2}V_3O_8$ exhibiting consistently higher Zn^{2+} diffusion coefficients than the comparison electrodes across the measured potential range (Equation S5). These $D_{Zn}{}^{2+}$ values are also well above those of typical vanadium-based cathodes (e.g., $ZnMn_2O_4$: 10^{-12}-10^{-13} cm^2 s^{-1} [46], δ-V_2O_5: 10^{-10}-10^{-11} cm^2 s^{-1} [47], etc. [39, 48]). These results collectively demonstrate that LC-$Ag_{1.2}V_3O_8$ enables rapid Zn^{2+} transport and low kinetic resistance, attributable to the combined effects of Ag-enabled electronic accessibility and defect-mediated diffusion pathways. LC-$Ag_{1.2}V_3O_8$ also demonstrates excellent rate capability (Figure 4f). Even at 3.0 A g^{-1} and 5.0 A g^{-1}, it retains 75.73% and 57.20% of its initial capacity, respectively. At an ultrahigh rate of 15 A g^{-1}, the electrode still delivers 199.16 mAh g^{-1}, and when the current density is reset to 0.5 A g^{-1}, the capacity fully recovers, indicating highly reversible Zn^{2+} storage.

First-principles calculations were employed to evaluate Zn^{2+} diffusion pathways and energy barriers for LC-$Ag_{1.2}V_3O_8$, HC-$Ag_{1.2}V_3O_8$, and HVO (Figures 4g and S34; Table S5). The calculated migration barriers follow the order LC-$Ag_{1.2}V_3O_8$ (0.69 eV) < HC-$Ag_{1.2}V_3O_8$ (1.16 eV) < HVO (1.57 eV), indicating that silver incorporation and structural disorder significantly lower the energy barrier for Zn^{2+} migration. The low-crystalline LC-$Ag_{1.2}V_3O_8$ offers a more flexible V-O framework and abundant disordered channels that accommodate ion hopping, whereas crystalline HC-$Ag_{1.2}V_3O_8$ is comparatively rigid and less adaptable [15]. Moreover, Zn^{2+} insertion energy profiles (Figure 4h) further reveal that LC-$Ag_{1.2}V_3O_8$ can accommodate more Zn^{2+} ions than crystalline HC-$Ag_{1.2}V_3O_8$. For LC-$Ag_{1.2}V_3O_8$, the stepwise insertion energies increase moderately from 0.83 to 1.55 eV as the number of Zn^{2+} ions rises from one to four, indicating smooth and energetically accessible insertion. By contrast, HC-$Ag_{1.2}V_3O_8$ shows a much steeper increase (0.22 to 2.05 eV), reflecting strong electrostatic repulsion and lattice rigidity. Such gradual energy variation in LC-$Ag_{1.2}V_3O_8$ implies that its disordered framework effectively buffers the local strain and electrostatic interactions induced by successive Zn^{2+} incorporation. This disorder-mediated structural flexibility, together with Ag-enabled electronic activation, explains why LC-$Ag_{1.2}V_3O_8$ can sustain substantially deeper and more reversible Zn^{2+} storage than HC-$Ag_{1.2}V_3O_8$ [49]. Therefore, the ultrahigh capacity of LC-$Ag_{1.2}V_3O_8$ originates from the synergistic contributions of bulk/near-surface Zn^{2+} storage, Ag/V dual-redox chemistry, and defect-assisted

15213773, 0, Downloaded from https://onlinelibrary.wiley.com/doi/10.1002/anie.3793292 by Hu linfeng - Southeast University , Wiley Online Library on [19/09/2026]. See the Terms and Conditions (https://onlinelibrary.wiley.com/terms-and-conditions) on Wiley Online Library for rules of use; OA articles are governed by the applicable Creative Commons License

pseudocapacitive charge storage, rather than from a simple extension of the conventional crystalline vanadate intercalation mechanism.

To assess possible proton participation in the aqueous electrolyte, comparative electrochemical measurements were performed using 1 M $Zn(CF_3SO_3)_2$ in water, 1 M $Zn(CF_3SO_3)_2$ in acetonitrile (AN), and an aqueous HOTf acidic control adjusted to pH 5.5 (Figure S35). The electrode retains most of its reversible capacity in the nonaqueous Zn^{2+}-containing electrolyte, whereas only a small capacity is observed in the HOTf control. These results support a Zn^{2+}-dominated storage mechanism with a limited proton contribution.

To further elucidate the redox evolution and structural response of LC-$Ag_{1.2}V_3O_8$ during cycling, ex situ XPS, in situ XRD, in situ Raman, and voltage-dependent impedance analyses were performed. Post-cycling XPS and EDS analyses revealed no detectable accumulation of Ag or V species on the Zn anode (Figures S36 and S37), suggesting the absence of appreciable crossover and deposition of cathode-derived species on the anode surface. Complementary ICP analysis further quantified the release of Ag and V into the electrolyte during the initial cycling at 0.1 A g^{-1}, with relatively low concentrations of both species detected in the bulk electrolyte (Table S6). Ex situ XPS was performed to track Zn^{2+} migration and vanadium redox behavior (Figures 5a–c and S38). In the pristine state, LC-$Ag_{1.2}V_3O_8$ is dominated by V^{5+}, consistent with the $[V_3O_8]^-$ framework. Upon discharging to 0.2 V vs. Zn^{2+}/Zn, Zn^{2+} intercalation reduces V^{5+} to V^{4+} and promotes the formation of oxygen vacancies, indicating a multi-electron redox mechanism [20]. The strongest defect-related signal observed at the maximum Zn^{2+} insertion state suggests that oxygen vacancies stabilize reduced vanadium species and facilitate Zn^{2+} accommodation. Meanwhile, the appearance of a metallic Ag° component in the Ag $3d_{5/2}$ region (~368.1 eV) indicates the partial reduction of Ag^+ to Ag^0 during deep discharge, demonstrating that Ag directly participates in the reversible redox process and serves as an additional charge-storage center. These results confirm that Ag is not merely retained in the framework, but directly participates in the reversible storage chemistry. The coupled Zn^{2+} storage process can tSherefore be schematically represented as:

$$\text{LC-Ag}_{1.2}\text{V}_3\text{O}_8 + x\text{Zn}^{2+} + 2x\text{e}^- \rightleftharpoons \text{Zn}_x\text{LC-Ag}_{1.2}\text{V}_3\text{O}_8$$

accompanied by the reversible redox transitions:

$$\text{Ag}^+ + \text{e}^- \rightleftharpoons \text{Ag}^0; \quad \text{V}^{5+} + \text{e}^- \rightleftharpoons \text{V}^{4+}$$

where LC-$Ag_{1.2}V_3O_8$ denotes the oxygen-vacancy-rich Ag-V-O host rather than an exact stoichiometric formula, and these equations are used only as schematic representations of Zn^{2+} insertion/extraction coupled with Ag/V redox transitions. The V^{5+}/V^{4+} transition is taken as the dominant vanadium redox process observed by ex situ XPS, while deeper V reduction may contribute at low potentials as suggested by electrochemical redox features.

The structural evolution of LC-$Ag_{1.2}V_3O_8$ during Zn^{2+} insertion/extraction was monitored by in situ XRD (Figures 5d and S39). The diffraction peaks of LC-$Ag_{1.2}V_3O_8$ remain visible throughout cycling, with no parasitic zinc hydroxide sulfonate formation (e.g., $Zn_4(OH)_6(CF_3SO_3)_2$), demonstrating the structural robustness of the low-crystalline LC-$Ag_{1.2}V_3O_8$ framework. During discharge, local strain induced by Zn^{2+} insertion shifts the diffraction peaks slightly, whereas charging allows the structure to relax, in accordance with Bragg's law (Equation S6) [6, 16, 18]. Reversible Ag^+/Ag^0-related reflections in the 36–40° region are consistent with reversible evolution of Ag species during cycling. The accompanying reversible diffraction-peak shifts further indicate a reversible structural response of the low-crystalline vanadate framework during Zn^{2+} insertion/extraction. In situ Raman spectra (Figures 5e and S40) further track local bonding changes during cycling. During the initial discharge from 1.2 to 0.5 V, the V═O band at ~1000 cm^{-1} decreases in intensity and broadens, reflecting Zn^{2+}-induced $V^{5+} \rightarrow V^{4+}$ reduction and accompanying local structural distortion. The V-O-V vibrations also shift reversibly, indicating temporary rearrangement and relaxation of the low-crystalline vanadate network during Zn^{2+} insertion. During early charging at ~0.5 V, Zn^{2+} extraction causes a ~2 cm^{-1} red shift of the V = O peak from 1037 to 1035 cm^{-1}, consistent with local structural relaxation observed by XRD (Equation S7). At approximately 1.7 V, the Raman bands largely recover toward their initial positions and spectral features, supporting reversible restoration of the local V-O coordination environment upon charging. These spectral changes closely track the galvanostatic profiles, demonstrating that the low-crystalline Ag-V-O network undergoes temporary local rearrangement during Zn^{2+} insertion and subsequently recovers upon Zn^{2+} extraction. Voltage-dependent impedance measurements (Figure 5f) further reveal the kinetic evolution of the electrode during cycling. The initial high R_s value (3.304 Ω) is associated with incomplete electrolyte wetting of the porous electrode and decreases to 1.219 Ω after repeated activation, indicating progressively improved charge transport. During discharge from 1.1 to 0.2 V, the impedance decreases as Zn^{2+} insertion and oxygen-vacancy formation facilitate ion migration. During charging from 0.2 to 1.7 V, the impedance increases slightly as the local structure relaxes. Notably, the impedance continuously decreases upon subsequent cycles, demonstrating that the low-crystalline LC-$Ag_{1.2}V_3O_8$ framework is dynamically adaptable and maintains efficient ion transport under repeated Zn^{2+} insertion/extraction.

3 | Conclusion

In summary, we have developed a low-crystalline silver-modified vanadate cathode (LC-$Ag_{1.2}V_3O_8$) that achieves ultrahigh-capacity and highly durable Zn^{2+} storage through the synergistic integration of redox-active Ag incorporation and short-range-ordered structural disorder. Comprehensive structural and spectroscopic analyses reveal that Ag incorporation reconstructs the local Ag-V-O coordination environment, induces partial V^{5+}/V^{4+} conversion, and lowers the oxygen-vacancy formation energy, while the low-crystalline framework stabilizes these defect-rich coordination environments and provides structurally adaptive pathways for Zn^{2+} transport. Together, these effects generate an oxygen-vacancy-rich Ag-V-O network with enhanced electronic accessibility, and reduced kinetic barriers for Zn^{2+} migration. Importantly, the defect-rich low-crystalline

15213773, 0, Downloaded from https://onlinelibrary.wiley.com/doi/10.1002/anie.3793292 by Hu linfeng - Southeast University , Wiley Online Library on [19/09/2026]. See the Terms and Conditions (https://onlinelibrary.wiley.com/terms-and-conditions) on Wiley Online Library for rules of use; OA articles are governed by the applicable Creative Commons License

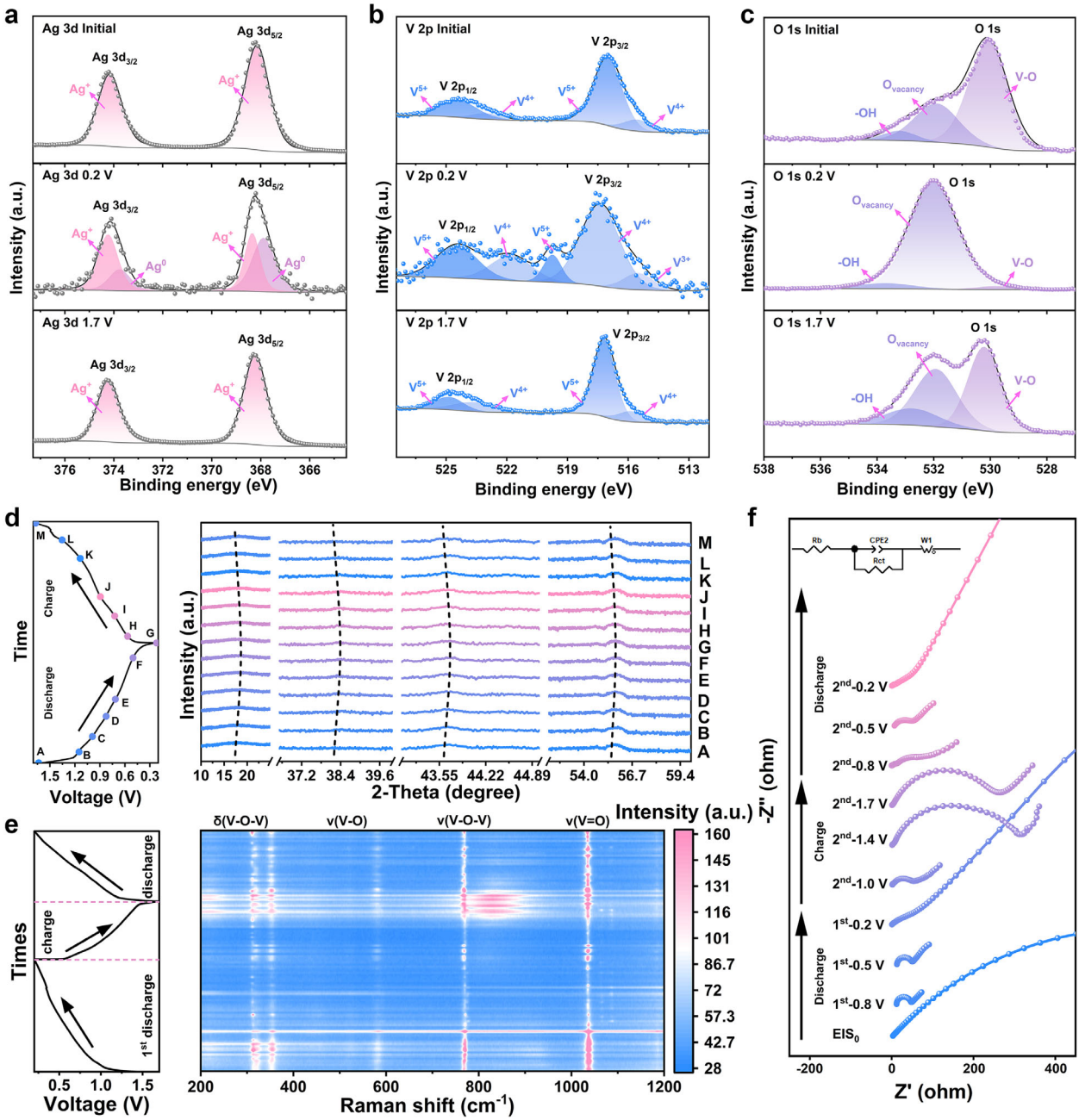

FIGURE 5 | Reaction mechanism investigation of the LC-$Ag_{1.2}V_3O_8$ electrode. High-resolution XPS spectra of (a) Ag 3d, (b) V 2p, and (c) O 1s for the LC-$Ag_{1.2}V_3O_8$ electrode at the initial, 0.2 V, and 1.7 V states. (d) GCD curves and in situ XRD patterns of LC-$Ag_{1.2}V_3O_8$ at 0.1 A g^{-1}. (e) GCD curves and in situ Raman spectra during the initial cycles at 0.1 A g^{-1}. (f) Ex situ EIS patterns of LC-$Ag_{1.2}V_3O_8$ (Inset: equivalent-circuit model used for fitting).

framework exposes abundant electrochemically accessible Ag-V-O active sites, promoting pseudocapacitive-dominated Zn^{2+} storage that bypasses the kinetic constraints of conventional bulk intercalation. Together with activated Ag/V dual-redox chemistry and accelerated Zn^{2+} transport, this enables deep and highly reversible utilization of otherwise inaccessible Ag/V redox sites. As a result, LC-$Ag_{1.2}V_3O_8$ delivers a reversible capacity of 525.51 mAh g^{-1} at 0.1 A g^{-1}, a record energy density of 499.23 Wh kg^{-1}, and exceptional cycling durability with nearly no capacity decay over 5,000 cycles at 8 A g^{-1}. More importantly, this work reveals how redox-active cation incorporation and structural disorder cooperatively reprogram local coordination environments, enabling simultaneous regulation of defect chemistry, redox accessibility, and Zn^{2+} transport. These findings highlight local coordination reprogramming as a promising materials-design strategy for low-crystalline Ag-containing vanadate cathodes and provide a mechanistic basis for further exploring related coordination-engineering approaches in aqueous Zn-ion storage.

Author Contributions

Hongxuan Tang: data curation, formal analysis, validation, writing – original draft. **Lixun Feng:** data curation, validation, methodology, formal analysis, visualization. **Xiaoyue Li:** formal analysis, data

15213773, 0, Downloaded from https://onlinelibrary.wiley.com/doi/10.1002/anie.3793292 by Hu linfeng - Southeast University , Wiley Online Library on [19/09/2026]. See the Terms and Conditions (https://onlinelibrary.wiley.com/terms-and-conditions) on Wiley Online Library for rules of use; OA articles are governed by the applicable Creative Commons License

curation, methodology. **Cuiqin Chao:** methodology, data curation, formal analysis, validation. **Longlong Tian:** data curation, investigation, methodology, formal analysis, visualization. **Xiaojun Gu:** data curation, formal analysis. **Jiahuan Zhao:** validation, formal analysis, investigation, visualization. **Xiaoying Liu:** methodology, validation, formal analysis, visualization, investigation. **Lifang Zheng:** investigation, formal analysis, resources, visualization. **Yuan Chen:** data curation, formal analysis. **Yan Zhao:** writing – review and editing, supervision, funding acquisition, conceptualization, validation. **Jiangwei Zhang:** validation, formal analysis, investigation. **Linfeng Hu:** formal analysis, validation, supervision, writing – review and editing, funding acquisition. **Limin Wu:** supervision, formal analysis, validation, funding acquisition, writing – review and editing.

Acknowledgments

This work is financially supported by the National Natural Science Foundation of China (52371214, 22375109, 22565022), Inner Mongolia Youth Science and Technology Talent Support Project (NJYT23001), the National Key Research and Development Program of China (2022YFA1205201), "Grassland Talents" of Inner Mongolia Autonomous Region, "Steed Plan High level Talents" of Inner Mongolia University, Graduate Research Innovation Project of Inner Mongolia (KC2024008S). We sincerely thank the School of Physics and Optoelectronic Engineering at Ludong University for granting access to the VASP software and the necessary computational facilities, which played a crucial role in supporting this research.

Conflicts of Interest

The authors declare no conflicts of interest.

Data Availability Statement

The data that support the findings of this study are available from the corresponding author upon reasonable request.

References

1. M. Liu, X. Li, M. Cui, et al., "Amorphous Organic-Hybrid Vanadium Oxide for Near-Barrier-Free Ultrafast-Charging Aqueous Zinc-Ion Battery," *Nature Communications* 15 (2024): 10769.

2. W. Ma, S. Wang, X. Wu, et al., "Tailoring Desolvation Strategies for Aqueous Zinc-Ion Batteries," *Energy & Environmental Science* 17 (2024): 4819–4846.

3. H. Meng, Q. Ran, T. Y. Dai, et al., "Lamellar Nanoporous Metal/Intermetallic Compound Heterostructure Regulating Dendrite-Free Zinc Electrodeposition for Wide-temperature Aqueous Zinc-Ion Battery," *Advanced Materials* 36 (2024): 2403803.

4. C. Zhang, Y. Huang, X. Xu, et al., "Bulk-to-surface co-modification of Layered Hydrated Vanadate Cathode for Aqueous Zinc Ion Batteries," *Energy & Environmental Science* 17 (2024): 4090–4103.

5. T. Lv, G. Zhu, S. Dong, et al., "Co-Intercalation of Dual Charge Carriers in Metal-Ion-Confining Layered Vanadium Oxide Nanobelts for Aqueous Zinc-ion Batteries," *Angewandte Chemie International Edition* 62 (2022): e202216089.

6. L. Wang, K.-W. Huang, J. Chen, and J. Zheng, "Ultralong Cycle Stability of Aqueous Zinc-Ion Batteries With Zinc Vanadium Oxide Cathodes," *Science Advances* 5 (2019): eaax4279.

7. T. Zhou, L. Xie, Q. Han, et al., "Progress and Prospect of Vanadates as Aqueous Zn-Ion Batteries Cathodes," *Coordination Chemistry Reviews* 498 (2024): 215461.

8. J. Guo, B. He, W. Gong, et al., "Emerging Amorphous to Crystalline Conversion Chemistry in Ca-doped VO_2 Cathodes for High-Capacity and Long-Term Wearable Aqueous Zinc-Ion Batteries"," *Advanced Materials* 36 (2024): 2303906.

9. Y. Dai, C. Zhang, J. Li, et al., "Inhibition of Vanadium Cathodes Dissolution in Aqueous Zn-Ion Batteries," *Advanced Materials* 36 (2024): 2310645.

10. M. Liao, J. Wang, L. Ye, et al., "A Deep-cycle Aqueous Zinc-ion Battery Containing an Oxygen-deficient Vanadium Oxide Cathode," *Angewandte Chemie International Edition* 59 (2019): 2273–2278.

11. K. Zhu, W. Jiang, Z. Wang, et al., "Hewettite $ZnV_6O_{16}{\cdot}8H_2O$ with Remarkably Stable Layers and Ultralarge Interlayer Spacing for High-performance Aqueous Zn-ion Batteries," *Angewandte Chemie International Edition* 62 (2023): e202213368.

12. J. Guan, L. Shao, L. Yu, et al., "Two-dimensional $Mg_{0.2}V_2O_5{\cdot}nH_2O$ Nanobelts Derived from V_4C_3 MXenes for Highly Stable Aqueous Zinc Ion Batteries"," *Chemical Engineering Journal* 443 (2022): 136502.

13. D. Zhao, X. Wang, W. Zhang, et al., "Unlocking the Capacity of Vanadium Oxide by Atomically Thin Graphene-analogous $V_2O_5{\cdot}nH_2O$ in Aqueous Zinc-Ion Batteries"," *Advanced Functional Materials* 33 (2023): 2211412.

14. S. K. Kang, M. Kim, H. H. Shin, et al., "Exceeding Theoretical Capacity in Exfoliated Ultrathin Manganese Ferrite Nanosheets via Galvanic Replacement-Derived Self-hybridization for Fast Rechargeable Lithium-Ion," *Advanced Functional Materials* 33 (2023): 2300143.

15. H. Song, Y.-F. Cui, Y. Li, et al., "Alcohol Molecule Coupling: A Universal Approach to Modulating Amorphousness in Vanadium-based Cathodes for High-rate and Durable Aqueous Zinc-Ion Batteries," *Science Advances* 11 (2025): eadt7502.

16. K. Yang, Y. Ying, L. Cui, et al., "Stable Aqueous Zn-Ag and Zn-Polyoxometalate Hybrid Battery Driven by Successive Ag^+ Cation and Polyoxoanion Redox Reactions," *Energy Storage Materials* 34 (2021): 203–210.

17. H. Liu, J. G. Wang, H. Sun, et al., "Mechanistic Investigation of Silver Vanadate as Superior Cathode for High Rate and Durable Zinc-ion Batteries," *Journal of Colloid and Interface Science* 560 (2020): 659–666.

18. F. Wan and Z. Niu, "Design Strategies for Vanadium-Based Aqueous Zinc-Ion Batteries," *Angewandte Chemie International Edition* 58 (2019): 16358–16367.

19. C. Li, R. Kingsbury, A. S. Thind, et al., "Enabling Selective Zinc-ion Intercalation by a Eutectic Electrolyte for Practical Anodeless Zinc Batteries," *Nature Communications* 14 (2023): 3067.

20. K. Fang, H. Zhang, P. Chen, et al., "Synergistic Structure Engineering and Electrochemical Activation Modulating Vanadium Oxide Cathode toward Superior Zinc-ion Storage," *Chemical Engineering Journal* 496 (2024): 153736.

21. Y. Peng, L. Mo, T. Wei, et al., "Oxygen Vacancies on $NH_4V_4O_{10}$ Accelerate Ion and Charge Transfer in Aqueous Zinc-Ion Batteries," *Small* 20 (2024): 2306972.

22. K. Ding, H. Zhang, J. Jiang, et al., "Balancing Carrier Dynamics in Oxygen-vacancy-tuned Amorphous Ga_2O_3 Thin-film Self-powered Photoelectrochemical-type Solar-blind Photodetector Arrays for Underwater Imaging," *Advanced Science* 11 (2024): 2407822.

23. H. Yi, A. Gao, X. Pang, et al., "Preparation of Single-Atom Ag-Decorated MnO_2 Hollow Microspheres by Redox Etching Method for High-Performance Solid-State Asymmetric Supercapacitors," *ACS Applied Energy Materials* 3 (2020): 10192–10201.

24. J. Wang, Z. Hou, X. Liu, et al., "Boosted Sodium Ion Storage Performance in MnO_2: Understanding the Bond Angle-Mediated Orbital Overlap in MnO_6 Units for Fast Charge Transfer," *Journal of Energy Chemistry* 87 (2023): 295–303.

25. H. Yadegari, Y. Li, M. N. Banis, et al., "On Rechargeability and Reaction Kinetics of Sodium-Air Batteries," *Energy & Environmental Science* 7 (2014): 3747–3757.

26. H. Huang, X. Xia, J. Yun, et al., "Interfacial Engineering of Hydrated Vanadate to Promote the Fast and Highly Reversible H^+/Zn^{2+} Co-

15213773, 0, Downloaded from https://onlinelibrary.wiley.com/doi/10.1002/anie.3793292 by Hu linfeng - Southeast University , Wiley Online Library on [19/09/2026]. See the Terms and Conditions (https://onlinelibrary.wiley.com/terms-and-conditions) on Wiley Online Library for rules of use; OA articles are governed by the applicable Creative Commons License

Insertion Processes for High-performance Aqueous Rechargeable Batteries," *Energy Storage Materials* 52 (2022): 473–484.

27. X. Wang, Y. Wang, A. Naveed, et al., "Magnesium Ion Doping and Micro-Structural Engineering Assist $NH_4V_4O_{10}$ as a High-Performance Aqueous Zinc Ion Battery Cathode," *Advanced Functional Materials* 33 (2023): 2306205.

28. D. Zhang, J. Cao, C. Yang, et al., "Highly Stable Aqueous Zn-Ion Batteries Achieved by Suppressing the Active Component Loss in Vanadium-Based Cathode," *Advanced Energy Materials* 15 (2024): 2404026.

29. X. Xie, N. Wang, S. Komarneni, and W. Hu, "Straw-sheaf-Like $AgVO_3$ Nanowires for Remarkable Zn^{2+} Storage Properties," *Colloids and Surfaces A: Physicochemical and Engineering Aspects* 690 (2024): 133755.

30. H. Lee, H. Lee, S. Baek, et al., "Unlocking Zinc Storage in Silver Vanadate Structures for High-Performance Aqueous Zinc Batteries," *Journal of Power Sources* 613 (2024): 234931.

31. T. Zhou, L. Xie, Q. Han, X. Yang, L. Zhu, and X. Cao, "Investigation of $Na_6V_{10}O_{28}$ as a Promising Rechargeable Aqueous Zinc-Ion Batteries Cathode," *Chemical Engineering Journal* 445 (2022): 136789.

32. T. Zhou, L. Zhu, L. Xie, et al., "New Insight on $K_2Zn_2V_{10}O_{28}$ as an Advanced Cathode for Rechargeable Aqueous Zinc-Ion Batteries," *Small* 18 (2022): 2107102.

33. K. Zhu, T. Wu, and K. Huang, "The Roles of Pre-inserted Dual-Cations and Structural Water in V_3O_8 Layer," *Advanced Energy Materials* 9 (2019): 1901968.

34. X. Guo, G. Fang, W. Zhang, et al., "Mechanistic Insights of Zn^{2+} Storage in Sodium Vanadates," *Advanced Energy Materials* 8 (2018): 1801819.

35. D.-S. Liu, Y. Zhang, S. Liu, et al., "Regulating the Electrolyte Solvation Structure Enables Ultralong Lifespan Vanadium-Based Cathodes with Excellent Low-temperature Performance," *Advanced Functional Materials* 32 (2022): 2111714.

36. Q. Li, Y. Liu, K. Ma, G. Yang, and C. Wang, "In Situ Ag Nanoparticles Reinforced Pseudo-Zn-Air Reaction Boosting $Ag_2V_4O_{11}$ as High-Performance Cathode Material for Aqueous Zinc-ion Batteries," *Small Methods* 3 (2019): 1900637.

37. Y. Zhang, F. Wan, S. Huang, S. Wang, Z. Niu, and J. Chen, "A Chemically Self-Charging Aqueous Zinc-Ion Battery," *Nature Communications* 11 (2020): 2199.

38. M. Li, X. Liu, J. Wu, X. Dong, Y. Wang, and S. Passerini, "Efficient and Effective Synthesis of $CaV_6O_{16}\cdot 2.7H_2O$ as High-Performance Cathode Material for Aqueous Zinc Metal Batteries," *Advanced Energy Materials* 15 (2025): 2404037.

39. Y. Liu, Q. Li, K. Ma, G. Yang, and C. Wang, "Graphene Oxide Wrapped CuV_2O_6 Nanobelts as High-Capacity and Long-Life Cathode Materials of Aqueous Zinc-Ion Batteries," *ACS Nano* 13 (2019): 12081–12089.

40. Y. Wang, S. Wang, L. Yang, F. Zhao, and H. Li, "A Facile Method for Pre-insertion of Cations and Structural Water in Preparing Durable Zinc Storage Vanadate Cathodes," *CrystEngComm* 24 (2022): 5487–5496.

41. F. Ming, H. Liang, Y. Lei, S. Kandambeth, M. Eddaoudi, and H. N. Alshareef, "Layered $Mg_xV_2O_5\cdot nH_2O$ as Cathode Material for High-Performance Aqueous Zinc Ion Batteries," *ACS Energy Letters* 3 (2018): 2602–2609.

42. C. Xia, J. Guo, P. Li, X. Zhang, and H. N. Alshareef, "Highly Stable Aqueous Zinc-Ion Storage Using a Layered Calcium Vanadium Oxide Bronze Cathode," *Angewandte Chemie International Edition* 57 (2018): 3943–3948.

43. Y.-H. Du, X.-Y. Liu, X.-Y. Wang, et al., "Freestanding Strontium Vanadate/Carbon Nanotube Films for Long-Life Aqueous Zinc-Ion Batteries," *Rare Metals* 41 (2021): 415–424.

44. T.-H. Wu, J.-A. Chen, W.-S. Lin, and W.-Y. Liang, "$La_{0.14}V_2O_5$/Reduced Graphene Oxide Composite for Aqueous Zinc-Ion Batteries With Long Cycle Life," *Journal of Electrochemical Society* 168 (2021): 080527.

45. Z. Wang, Y. Song, J. Wang, et al., "Vanadium Oxides With Amorphous-Crystalline Heterointerface Network for Aqueous Zinc-Ion Batteries," *Angewandte Chemie International Edition* 62 (2023): e202216290.

46. K. Cai, S.-H. Luo, J. Cong, et al., "Synthesis and Optimization of $ZnMn_2O_4$ Cathode Material for Zinc-Ion Battery by Citric Acid Sol-Gel Method," *Journal of The Electrochemical Society* 169 (2022): 030531.

47. X. Liu, H. Euchner, M. Zarrabeitia, et al., "Operando pH Measurements Decipher H^+/Zn^{2+} Intercalation Chemistry in High-Performance Aqueous Zn/δ-V_2O_5 Batteries," *ACS Energy Letters* 5 (2020): 2979–2986.

48. W. Zhong, R. Zhao, Y. Zhu, Y. Xu, W. Chen, and C. Peng, "Vacancy Engineering on MnSe Cathode Enables High-Rate and Stable Zinc-Ion Storage," *Advanced Functional Materials* 35 (2024): 2419720.

49. J. Sun, J. Yang, Y. Zhang, et al., "Reduced Graphene Oxide Pre-Intercalation Enables Double-Sided Zn^{2+} Storage Between VO Layers in $V_2O_5\cdot nH_2O$," *Energy Storage Materials* 83 (2025): 104696.

Supporting Information

Additional supporting information can be found online in the Supporting Information section.

Supporting File: anie74893-sup-0001-SuppMat.docx.

15213773, 0, Downloaded from https://onlinelibrary.wiley.com/doi/10.1002/anie.3793292 by Hu linfeng - Southeast University , Wiley Online Library on [19/09/2026]. See the Terms and Conditions (https://onlinelibrary.wiley.com/terms-and-conditions) on Wiley Online Library for rules of use; OA articles are governed by the applicable Creative Commons License